Macromolecules

Article

pubs.acs.org/Macromolecules

Modulating Crystallinity of Poly(3-hexylthiophene) via Microphase Separation of Poly(3-hexylthiophene)−Polyisoprene Block Copolymers

Herman Lim,[†] Chi-Yang Chao,*[,†] and Wei-Fang Su[†,‡]

[†]Department of Materials Science and Engineering and [‡]Institute of Polymer Science, National Taiwan University, Taipei City, Taiwan 10617

Supporting Information

ABSTRACT: A series of poly(3-hexylthiophene)-*block*-polyisoprene (P3HT-*b*-PI) diblock copolymers (DBCP) and polyisoprene-*block*-poly(3-hexylthiophene)-*block*-polyisoprene (PI-*b*-P3HT-*b*-PI) triblock copolymers (TBCP) with accurately controlled molecular architecture were synthesized via highly efficient coupling reaction between aldehyde end-functionalized P3HT and living anionic polyisoprene. The self-assembly behaviors, considering morphology and crystallinity, of the thermal annealed bulk samples of these DBCPs and TBCPs containing various PI content were systematically investigated. The DBCPs behaved very differently from most published P3HT BCP systems, showing elongated fibers with preserved crystallinity regardless of the PI fraction. More noteworthy, with PI fraction less than 40 wt %, the DBCPs exhibited parallel straight fibers longer than several micrometers accompanied by concurrent enhanced crystallinity. The unique microstructure of the DBCPs might originate from moderate microphase separation between P3HT and PI as well as high flexibility of PI to conduct the packing of P3HT. The TBCPs, by contrast, exhibited highly curved interdomain boundaries with significant depressed crystallinity, resembling P3HT diblock copolymers in the strong phase segregation regime, as more pronounced entanglement of the two terminal PI segments would restrict the movement of P3HT.

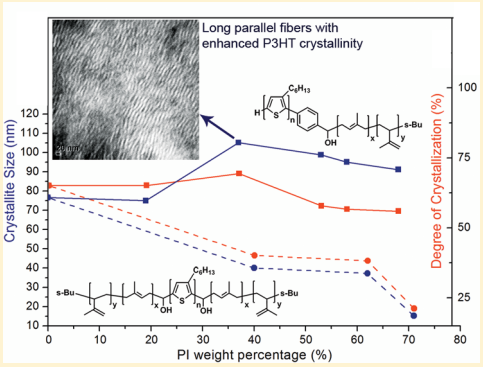

INTRODUCTION

Poly(3-hexylthiophene) (P3HT), the mostly studied conjugated polymer, has been investigated widely for its good potential in the applications of organic electronic devices, such as solar cells, field emission transistors, light-emitting devices, and sensors.[1−7] The performance of these P3HT based devices was found to be significantly affected by the optical and electronic properties of P3HT, which were closely related to its microstructure and crystallinity governed complicatedly by crystallization behaviors of P3HT. Owing to the semicrystalline nature of P3HT, a wide variety of factors, including the intrinsic properties of P3HT such as the molecular weight and the regioregularity as well as the processing parameters, would affect crystallization of P3HT and thus the resulting morphology of P3HT within the active component.

In most P3HT samples, fast crystallization of P3HT generally results in randomly oriented short fibers with numerous grain boundaries to limit the charge mobility. To enhance the charge mobility, optimizing the microstructure by concurrently elongating the fibers and increasing the crystallinity of P3HT was highly desired yet difficult to be achieved. Several approaches have been reported to improve the crystallinity of P3HT by promoting chain movements of P3HT via thermal annealing[8] and solvent annealing[9] to allow better packing. Nevertheless, the enhancements in enlarging the crystallite size and in elongating the fibers of P3HT were limited owing to the difficulty to move the P3HT crystallites. Efforts using temperature control[10−12] and solubility alternation[13] to promote aggregation of P3HT crystals in solution were also reported to enhance the degree of crystallization of P3HT, but the processing parameters were difficult to control practically.

An alternative approach to manipulate the microstructure and the crystallinity of P3HT is the use of P3HT block copolymers (BCPs). By connecting one or two coil segment(s) to the terminal(s) of P3HT via covalent bonding, microphase separation between P3HT and the coil segment should substantially affect the assembly of P3HT and thus provide a good opportunity to achieve desirable morphologies through suitable processing. When aiming for long P3HT fibers, P3HT-*b*-PLLA (poly(3-hexylthiophene)-*b*-polylactide), for example, exhibited parallel aligned straight strips with several hundred nanometers long in the spin-coated thin films.[14,15] Nevertheless, microphase separation would interfere with crystallization of P3HT so that most of the P3HT BCPs reported in the literature exhibited hampered crystallinity. In addition, a coil segment with relatively high glass transition temperature (e.g., poly(methyl methacrylate), polystyrene, and poly(vinylpyridine)) would also restrict the molecular movement

Received: December 17, 2014
Revised: April 15, 2015
Published: May 12, 2015

DOI: 10.1021/ma502417w
Macromolecules 2015, 48, 3269−3281

Scheme 1. Syntheses of P3HT-H/CHO and P3HT-CHO/CHO

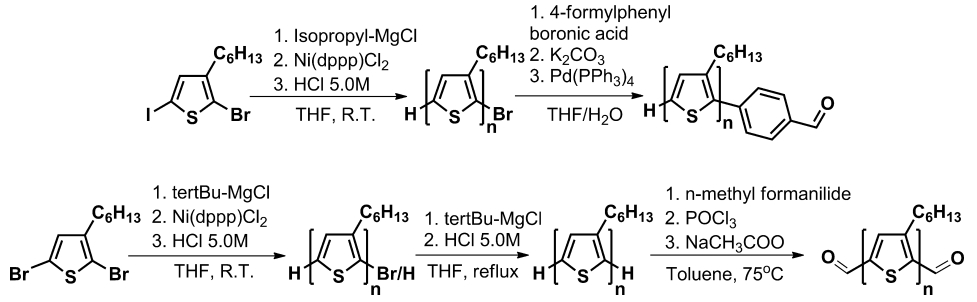

Scheme 2. Syntheses of P3HT-*b*-PI and PI-*b*-P3HT-*b*-PI by the Coupling Method

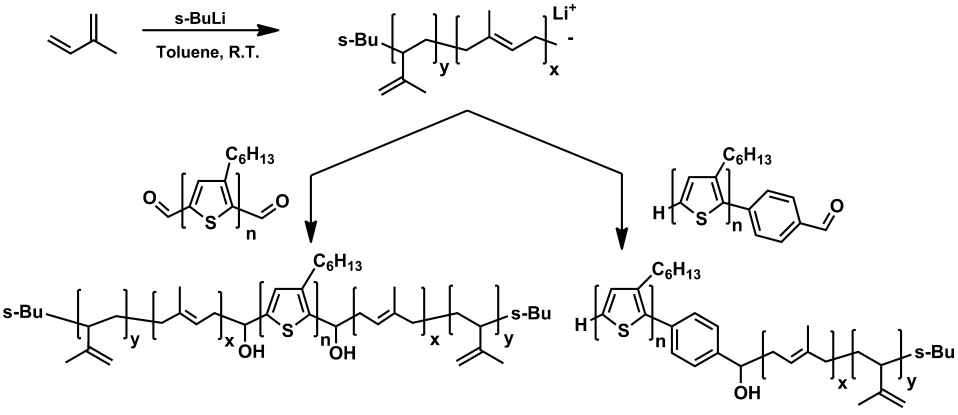

to prevent ordered packing of P3HT.[16−18] Hence, selecting suitable coil segment and building the BCP with appropriate architecture are critical to manipulate self-assembly of P3HT BCPs toward desirable microstructure with concurrent enhanced crystallinity.

In this work, polyisoprene (PI) was employed for the coil segment as moderate microphase separation between P3HT and PI would not overwhelm crystallization of P3HT while high flexibility of PI could enhance molecular mobility to allow ordered packing of P3HT. Very limited works related to P3HT-PI BCPs have been reported which suggested that PI could potentially modulate the packing of P3HT toward better organization. For example, our previous work demonstrated polyisoprene-*block*-poly(3-hexylthiophene)-*block*-polyisoprene (PI-*b*-P3HT-*b*-PI) triblock copolymers would enhance $\pi-\pi$ stacking of P3HT in the spin-coated thin film as compared to the pristine P3HT.[19,20] Deribew et al. utilized P3HT-*b*-PI diblock copolymers as compatibilizers in P3HT/PCBM bulk heterojunction solar cells to alter the crystallization of P3HT, leading to improved photovoltaic performance.[21] Hereby, we aimed to synthesize P3HT-*b*-PI diblock and PI-*b*-P3HT-*b*-PI triblock copolymers with various compositions and to systematically explore the assembly behaviors of these BCPs. Upon comprehensively understanding interplays between morphology and crystallinity, long P3HT fibrils with improved crystallinity could be achieved by optimizing the molecular architecture of the P3HT-PI BCPs.

Well-defined P3HT-*b*-PI diblock and PI-*b*-P3HT-*b*-PI triblock copolymers, denoted as DBCPs and TBCPs, respectively, in this work, were synthesized via efficient coupling reaction between aldehyde end-functionalized P3HT and living polyisoprene anions.[19] Through this method, accurate control on molecular weights and compositions of both DBCPs and TBCPs was achieved. The weight fraction of the PI segment in TBCPs matched that in DBCPs intentionally to investigate the effect of molecular arrangement. WAXS and DSC were carried out to evaluate the crystallinity while TEM and SAXS studies were performed to identify the morphological information. It was found that a short PI in DBCPs could facilitate elongated straight strips with enhanced P3HT crystallinity. Nevertheless, longer PI in DBCPs resulted in stronger microphase separation, leading to curved fibers with slightly suppressed crystallinity of P3HT. The crystallinity of P3HT in TBCPs was further suppressed to form short fibers and cylinders owing to more pronounced entanglement of two terminal PIs in TBCPs, which would severely restrict the chain movement of P3HT.

RESULTS AND DISCUSSION

Synthesis of P3HT-*b*-PI Diblock Copolymers and PI-*b*-P3HT-*b*-PI Triblock Copolymers. P3HT-PI diblock and triblock copolymers with high purity and narrow molecular weight distribution were synthesized via efficient coupling reaction between aldehyde end-functionalized P3HT and living polyisoprene anions. Schemes 1 and 2 illustrate the aldehyde end-functionalization of P3HT and the synthetic routes for the block copolymers, respectively. To achieve accurate control on the molecular architecture of these block copolymers, successful end-functionalization of regioregular P3HT to afford high purity of end groups is critical. Highly regioregular P3HT, generally synthesized via the GRIM method,[22−24] possesses three kinds of end groups: H/Br (a hydrogen at one end and a bromine at the other end) as the majority alone with H/H (hydrogens at both ends) and Br/Br (bromines at both ends) as the minority. P3HT-H/Br is needed for diblock copolymers while P3HT-H/H is suitable for ABA type triblock copolymers through further selective end-group modification. In this work,

DOI: 10.1021/ma502417w
Macromolecules 2015, 48, 3269−3281

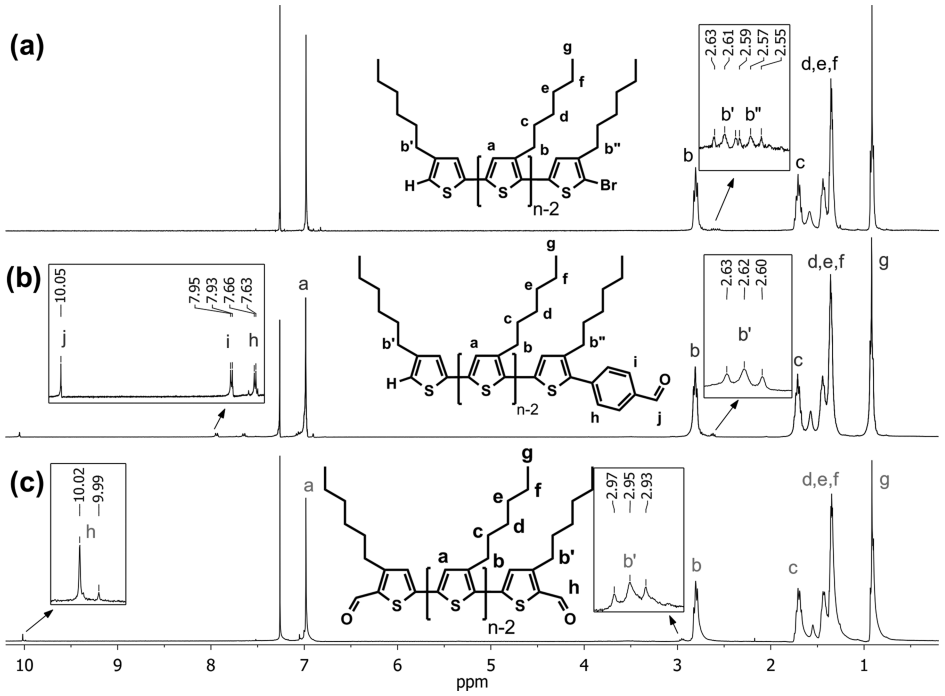

Figure 1. ^{1}H NMR spectra of (a) P3HT-H/Br, (b) P3HT-H/CHO, and (c) P3HT-CHO/CHO in *d*-chloroform. The insets signify the details of chemical shifts corresponding to the end-groups.

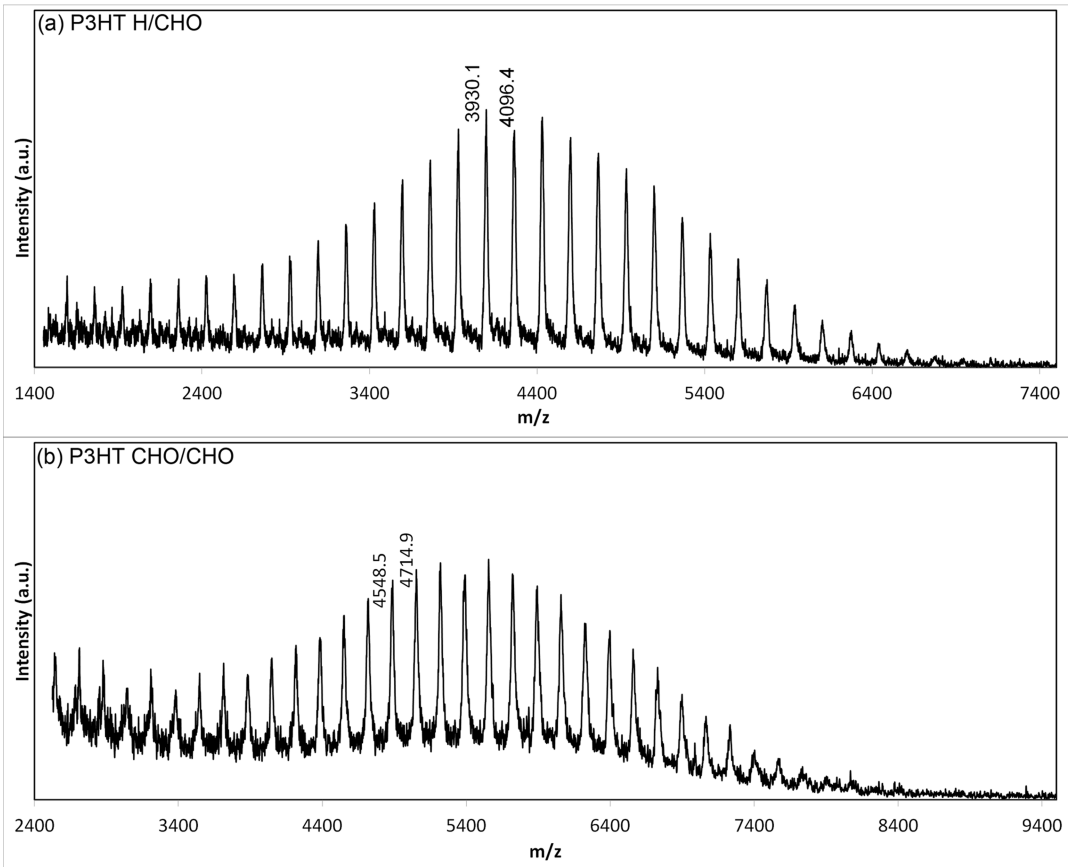

Figure 2. MALDI-TOF-MS spectra of (a) P3HT-H/CHO and (b) P3HT-CHO/CHO.

P3HT-H/Br was obtained from Yokozawa method instead of commonly used GRIM method owing to better control on the end groups.[24,25] The key to successful end group control was the use of 0.95 equiv (instead of 1 equiv) of isopropylmagnesium chloride to activate the monomer 2-bromo-3-hexyl-5-iodothiophene to ensure the absence of unreacted Grignard

DOI: 10.1021/ma502417w
Macromolecules 2015, 48, 3269−3281

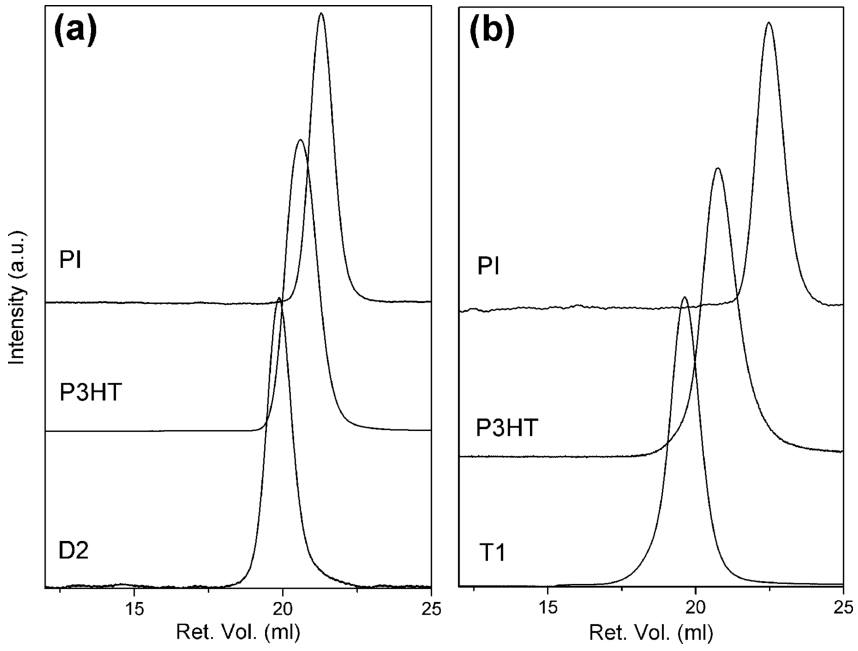

Figure 3. GPC traces (RI signal) of (a) D2 and (b) T1 and the corresponding constituent homopolymers.

Table 1. Molecular Weight, Polydispersity Index (PDI), and Number of Repeat Unit (N) of P3HT-PI BCPs and the Corresponding Building Blocks

	P3HT		PI[b]		block copolymers	
polymer	M_n (PDI)[a]	N	M_n (PDI)[a]	N	M_n (PDI)[a]	PI (wt %)[c]
D1	7500 (1.13)	45	2600 (1.08)	38	11000 (1.10)	19
D2	7500 (1.13)	45	5700 (1.06)	84	14000 (1.12)	38
D3	7500 (1.13)	45	9100 (1.07)	134	16900 (1.15)	50
D4	7500 (1.13)	45	12400 (1.06)	182	18600 (1.19)	58
D5	7500 (1.13)	45	18300 (1.07)	269	22900 (1.25)	68
T1	7500 (1.16)	45	3000 (1.08)	44	14800 (1.18)	40
T2	7500 (1.16)	45	6200 (1.07)	91	20900 (1.20)	62
T3	7500 (1.16)	45	11700 (1.06)	172	31900 (1.26)	71

[a]Obtained from GPC measurements. [b]M_n and N of PI in T1−T3 represent only one of the two terminal PI segments. [c]Calculated from ^{1}H NMR of the block copolymers.

reagent before the polymerization takes place.[26] Benzaldehyde was then attached to the bromine terminal of P3HT via Suzuki coupling between the Br terminal of P3HT and 4-formylphenylboronic acid in high yield to afford mono-end-functionalized P3HT (P3HT-H/CHO) with high purity. P3HT with both terminals capped with aldehydes (P3HT-CHO/CHO) were synthesized according to our previous work.[19]

The high purity of aldehyde end-functionalized P3HT was confirmed by ^{1}H NMR and MALDI-TOF-MS studies. Figure 1 depicts the ^{1}H NMR spectra of P3HT-H/Br, P3HT-H/CHO, and P3HT-CHO/CHO. For P3HT H/Br (Figure 1a), two sets of triplet peaks assigned to $H_{b'}$ and $H_{b''}$ of the two terminal thiophene rings were clearly observed because of two distinctive chemical environments, which were also different from H_b in the central thiophene rings. In P3HT-H/CHO (Figure 1b), the triplet peak at 2.57 ppm corresponding to $H_{b''}$ in P3HT-H/Br completely disappeared since $H_{b''}$ hereafter experienced similar chemical environment as H_b in the central thiophene rings did. The signals appeared at 10.05 ppm in P3HT-H/CHO further suggested the presence of aldehyde in P3HT-H/CHO. In Figure 1c for P3HT-CHO/CHO, the appearance of the aldehyde signals at 10.02 ppm (2-position of the terminal thiophene ring) and 9.99 ppm (5-position of the terminal thiophene ring)[27] as well as the shift of the triplet peak for $H_{b'}$ from 2.61 ppm in P3HT-H/H (^{1}H NMR spectra is provided in the Supporting Information) to 2.95 ppm suggested the success in the formylation reactions.

Figures 2a and 2b show the MALDI-TOF-MS spectra of P3HT-H/CHO and P3HT-CHO/CHO, respectively. In both spectra, only one set of peaks was observed, and the difference between two contagious peaks is 166.2 Da, very close to the molar mass of a 3HT repeating unit. The peak values in Figure 2a were equal to (n × 166.2) + 1 + 106.9 (e.g., 4096.4 Da), which were identical to the theoretical molecular weights of P3HT-H/CHO. On the other hand, the peak values in Figure 3b were assigned to (n × 166.2) + 29 + 29 (e.g., 4714.9 Da), equal to the theoretical formula weights of P3HT-CHO/CHO. The cleanness of the MALDI-TOF-MS spectra and the good matches between the measured molecular weights and the theoretical ones further confirm the high purity of P3HT-H/CHO and P3HT-CHO/CHO.

Fast kinetics of polymerization and high reactivity of living polymeric anions toward aldehyde group are two main considerations to adopt anionic polymerization to synthesize

DOI: 10.1021/ma502417w
Macromolecules 2015, 48, 3269−3281

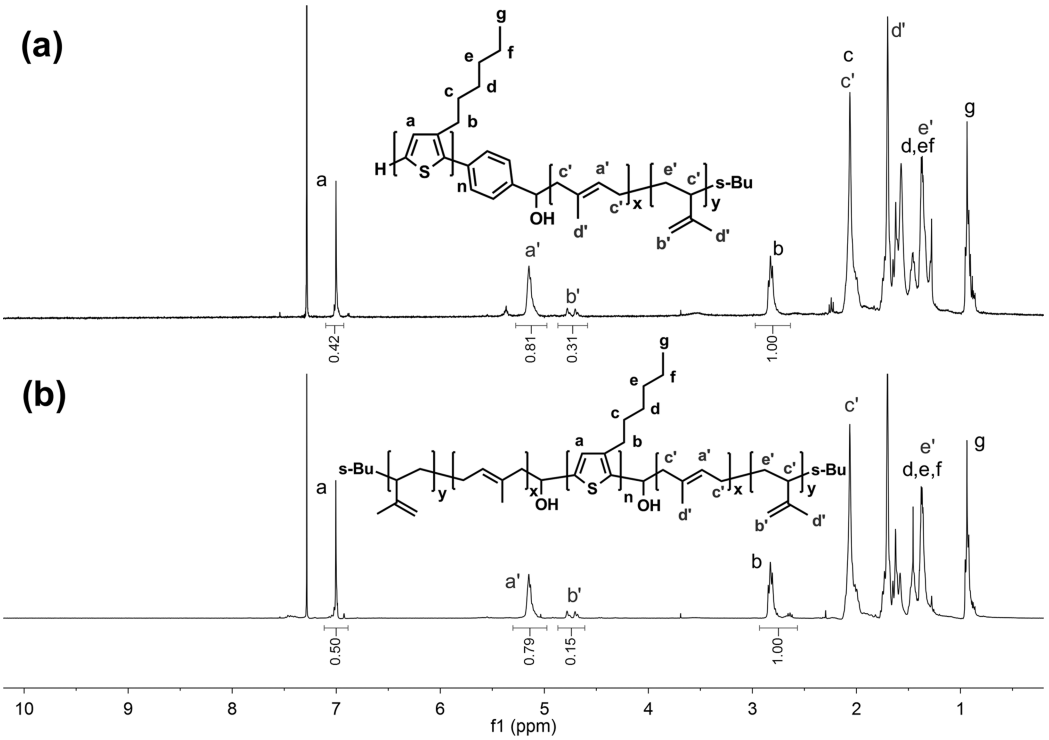

Figure 4. ^{1}H NMR of (a) D2 and (b) T1 in *d*-chloroform.

polyisoprene segment. The coupling method enables each building block with accurately controlled molecular weight to be synthesized individually to produce block copolymers having designated compositions. In our previous work,[19] the coupling reaction between the terminal aldehyde of P3HT-CHO/CHO and various polymeric anions has been demonstrated to be effective and which could successfully afford P3HT triblock copolymers with different coil segments. In this work, DBCPs could also be successfully prepared via similar methodology using mono-end-functionalized P3HT-H/CHO. To ensure the completeness of the coupling reaction, excess living polyisoprene anions (5 equiv) were used and which should simplify the purification by removing only the excess polyisoprene.

Table 1 summarizes the compositions of all the synthesized block copolymers as well as the number of repeat unit and the molecular weight of the corresponding building blocks. DBCPs and TBCPs were named as DX and TX, respectively. The GPC traces of D2 and T1 as well as the corresponding P3HT homopolymers and PI homopolymers are shown in Figure 3 as representative cases. The monomodal molecular weight distribution in the GPC trace of D2 and the low polydispersity (1.12) suggest the success of coupling reaction as well as the purity of the final product. All synthesized block copolymers exhibited monomodal molecular weight distribution with low polydispersity, indicating the coupling reaction was successful for all the range of molecular weight in this work (see Figure S1 in the Supporting Information for GPC traces of all BCPs). Furthermore, no aldehyde peak around 10 ppm could be detected in the ^{1}H NMR spectra of D2 and T1 as illustrated in Figures 4a and 4b, which further confirmed the completeness of the coupling reaction between the aldehyde end groups at P3HT and the living polyisoprene anions.

Morphology of Thermal Annealed Bulk Samples. The morphologies of the thermal annealed bulk samples of block copolymers were identified by TEM images and SAXS patterns presented in Figure 5. The bright areas in the TEM images represent P3HT-rich domains while the dark areas suggest PI-rich domains. During the thermal annealing process, the solvent-cast samples were first heated above the melting point (>230 °C) of P3HT to allow kinetically trapped P3HT segments to move freely, and the melt samples appeared orange to ensure complete isotropy. The melts were then cooled down to 185 °C and annealed for 24 h under vacuum, a temperature slightly above the crystallization temperature of P3HT and well above the T_g of PI. The annealed samples were then slowly cooled to room temperature under vacuum. DBCPs containing lower weight fraction of PI (<40 wt %), including D1 and D2, exhibited lamellar morphologies with straight and extended interdomain boundaries (IDBs) in the TEM images. The characteristic scattering signals of lamellae were observed in the SAXS patterns, suggested by the appearance of two peaks with q_1:q_2 = 1:2, to further confirm the existence of lamellae. The thickness of a lamellae was determined by $d = 2\pi/q_1$ from the SAXS pattern, suggesting d = 16 nm for D1 and d = 21 nm for D2, which are close to the periodicity observed from the TEM images. With increasing weight fraction of PI, D3, D4, and D5 formed shorter fibers with curved IDBs as suggested by the TEM images. The corresponding SAXS patterns exhibited one broad peak with relative weak intensity at low q range, indicating the lack of uniform periodicity in the microstructure. The morphological disorderliness was found to increase with increasing PI length. A broad scattering signal at higher q range was also observed for D3, D4, and D5, which could be attributed to the P3HT fibers as the corresponding d-spacing (~10 nm) was close to the calculated contour length (~9 nm) of a fully stretched P3HT. It was noticed that the d-spacing of this high q signal was almost identical in D3, D4, and D5, suggesting extensive elongation of PI should trivially affect the packing of P3HT. For TBCPs, shorter PI in T1 resulted in lamellar morphology while increasing fraction of PI in T2 and

DOI: 10.1021/ma502417w
Macromolecules 2015, 48, 3269−3281

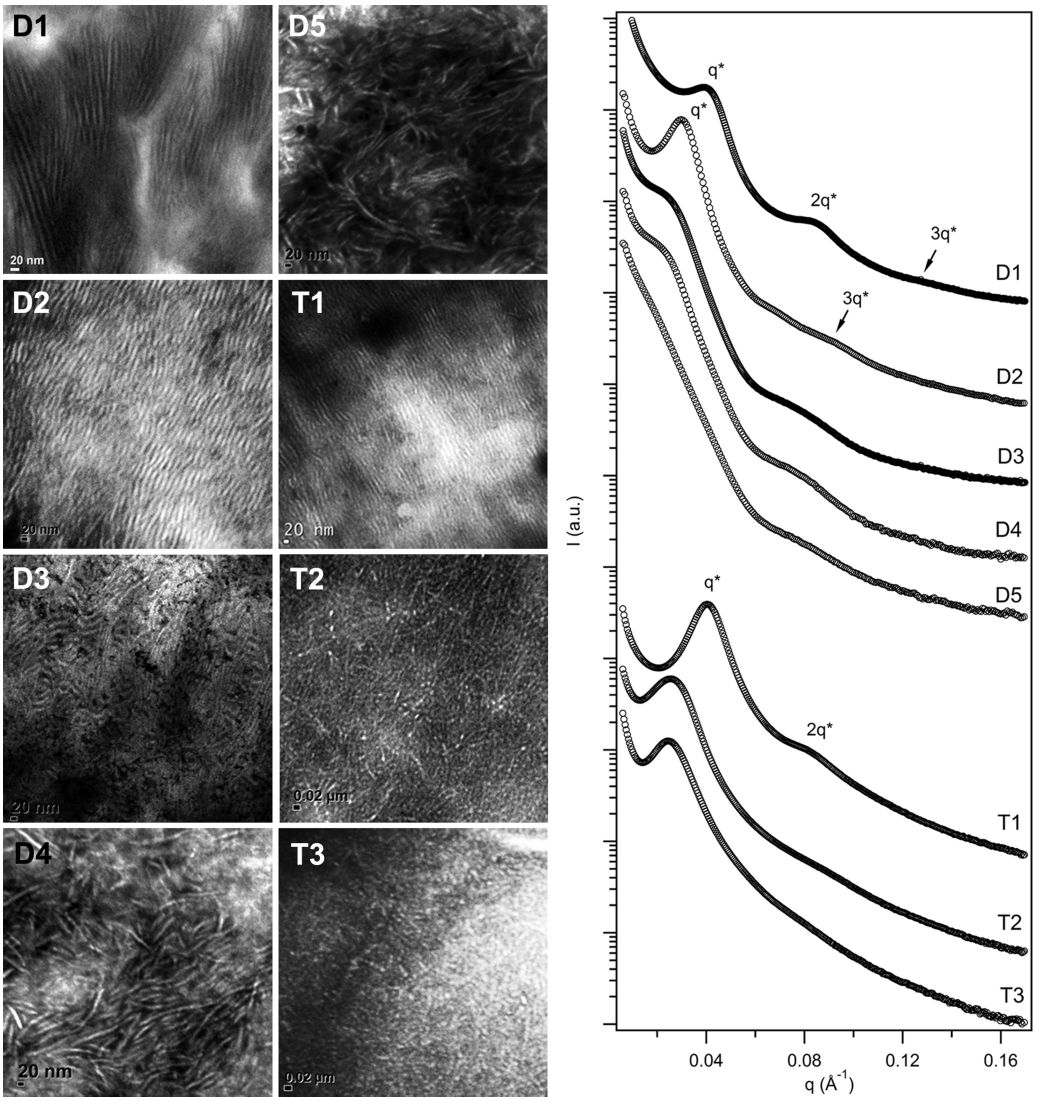

Figure 5. TEM images and SAXS profiles of the thermal annealed bulk samples of P3HT-PI BCPs.

T3 led to short P3HT fibers and cylinders embedded in PI matrix as suggested by the small circular white spots in the TEM images. Considering T1 and D2 possessing similar weight fraction of PI, the thickness of a lamellae in T1 suggested by the SAXS pattern was 15 nm, obviously smaller than that in D2. The white strips, representing P3HT domains, in the TEM image of T1 appeared much thinner than those of D2. The presence of only one broad peak in the corresponding SAXS patterns of T2 and T3 also indicates the irregular arrangement of the microstructure. The above observations indicate PI in TBCPs would considerably interfere the packing of P3HT, and further elongation of PI could significantly hamper the crystallization of P3HT, leading to highly curved domain boundaries of P3HT. The statements addressing the crystallinity will be further confirmed by the crystallinity studies discussed in the following section.

Crystallinity of P3HT in the BCPs. To understand the effect of PI on the crystallinity of the P3HT domains, WAXS measurements were performed to evaluate the crystal structure and the diffraction patterns are illustrated in Figure 6. The lattice parameters of a P3HT crystallite and the average crystallite size retrieved from the WAXS patterns are summarized in Table S1.

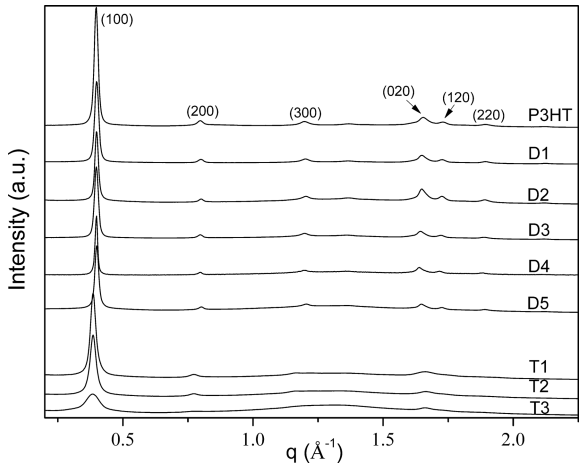

Figure 6. WAXS patterns of the P3HT-PI BCPs and the pristine P3HT homopolymer.

In all DBCPs, the crystalline structure of P3HT was preserved as D1−D5 exhibited WAXS patterns similar to that of the pristine P3HT despite of the attenuation in intensity due

DOI: 10.1021/ma502417w
Macromolecules 2015, 48, 3269−3281

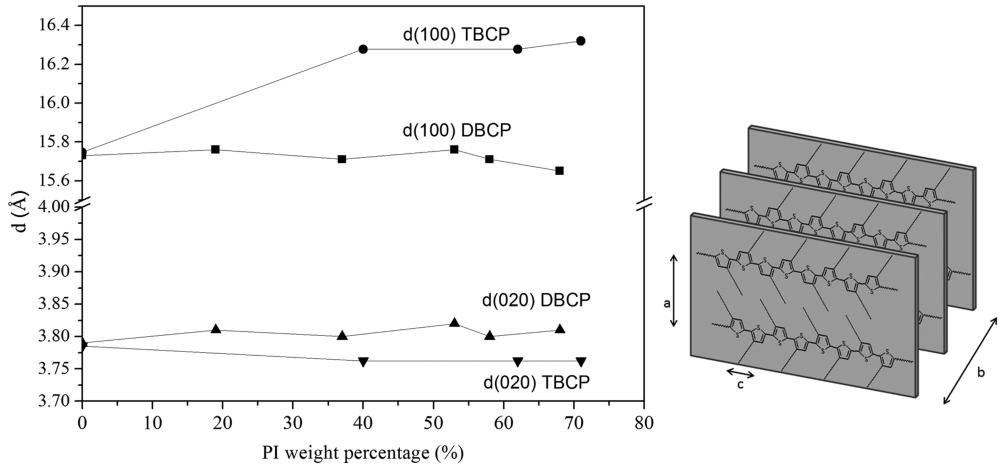

Figure 7. $d(100)$ and $d(020)$ of DBCPs and TBCPs as well as schematic illustation of the lattice parameters of a P3HT crystal.

to the decreasing P3HT content in the block copolymers. Peaks of higher order (h00) could also be clearly observed in all DBCPs but hardly seen in TBCPs. In addition, the (020) diffraction peak in TBCPs became much broader alone with the appearance amorphous halo around q = 1.0−1.5. Figure 7 shows the d-spacings along (100) and (020) directions, denoted as $d_{(100)}$ and $d_{(020)}$, respectively, corresponding to the lattice parameter a and b in a unit cell of P3HT. $d_{(100)}$ remained almost unchanged for DBCPs with increasing PI content while a noticeable enlargement in $d_{(100)}$ was observed for TBCPs as compared to the pristine P3HT. By contrast, the variation in $d_{(020)}$ was trivial for both DBCPs and TBCPs. The crystallite size of P3HT in (100) direction was estimated from Scherer's formula based on the full width at half-maximum (fwhm) of the corresponding peak. Figure 8 depicts the relation of the

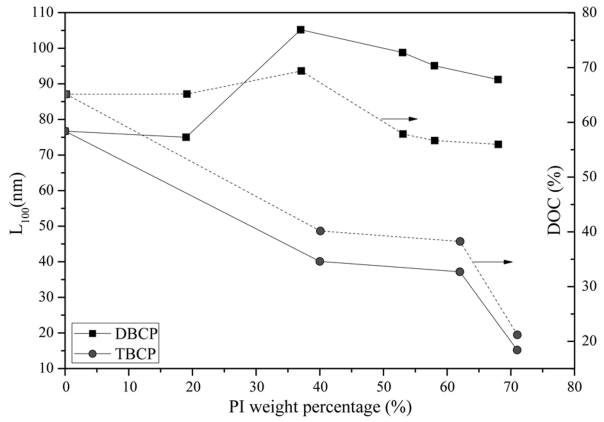

Figure 8. Crystallite size (corresponding to L100) and the degree of crystallization (DC) against the weight fraction of PI in BCPs.

crystallite size against the PI content in BCPs. Surprisingly, the crystallite sizes of P3HT in most DBCPs were even larger than that of the pristine P3HT except D1, whose crystallite size was comparable to the pristine P3HT. A remarkable 37% improvement in the crystallite size with respect to the pristine P3HT was observed for D2, which was larger than 100 nm. For TBCPs, the crystallite size was apparently smaller than that of the pristine P3HT and which decreased with increasing PI content. These observations suggested that the attachment of PI to P3HT in DBCPs should not alter the intermolecular stacking of P3HT and which could further enhance the growth of P3HT crystallites. By contrast, the presence of PI in TBCPs would significantly affect the crystal structure by increasing the intermolecular distance along the direction of side-chain interdigitation and depress the crystallinity.

To further investigate the crystallization and melting behaviors of P3HT within the copolymers as well as the degree of crystallization (DC), differential scanning calorimetry (DSC) was studied on the thermal annealed samples, and the DSC curves of DBCPs and TBCPs are presented in Figures 9a and 9b, respectively. The temperatures of phase transitions and DC are also summarized in Table S1. Upon first heating, two endothermic transitions were found. The first transition appeared between 33 and 71 °C, denoted as H(I), should associate with the rearrangement of hexyl side chains of P3HT.[28−30] The second transition located between 130 and 211 °C, labeled as H(II), was assigned to the phase transition from a two-dimensional crystal to an isotropic liquid.[31,32] H(II) could be further detailed into three subtransitions, which are denoted as transitions a, b, and c from low to high temperature. According to the literature, transition a refers to a smectic−smectic transition and transition b indicates the phase transition from a two-dimensional smectic-like molecular packing to a highly mobile nematic phase, while transition c represents the clearing transition to isotropic phase.[32]

For H(I), DBCPs exhibited transition temperatures similar to that of the pristine P3HT while TBCPs' transitions were apparently lower, even approaching room temperature. The significantly lowered H(I) in TBCPs could be attributed to the suppression in crystallite size and the looser interdigitation of hexyl side chains. For H(II), whose peak temperatures of the subtransitions against the weight fraction of PI in the BCPs are illustrated in Figure 10, the most noteworthy differences between BCPs and the pristine P3HT are (1) significantly elevated temperature of transition b in BCPs and (2) the increasing relative intensity of transition b to transition c, i.e., $\Delta H_b/\Delta H_c$. These observations suggested that the presence of PI might encourage the nematic phase between transitions b and c, which was unfeasibly achieved by the pristine P3HT.[32−34] Unfortunately, the existence of nematic phase could not be detected by polarized optical microscopy owing to the narrow temperature range. The remarkable elevation of the temperature of transition b further suggests the postponed melting of the P3HT crystallites, probably due to the increasing

DOI: 10.1021/ma502417w
Macromolecules 2015, 48, 3269−3281

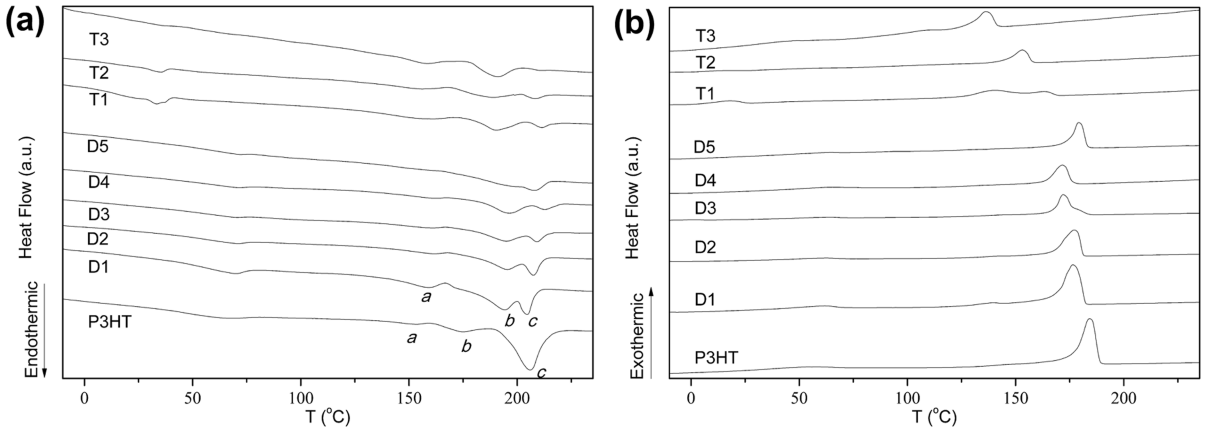

Figure 9. DSC traces (a) first heating cycle and (b) first cooling cycle of thermal annealed BCPs.

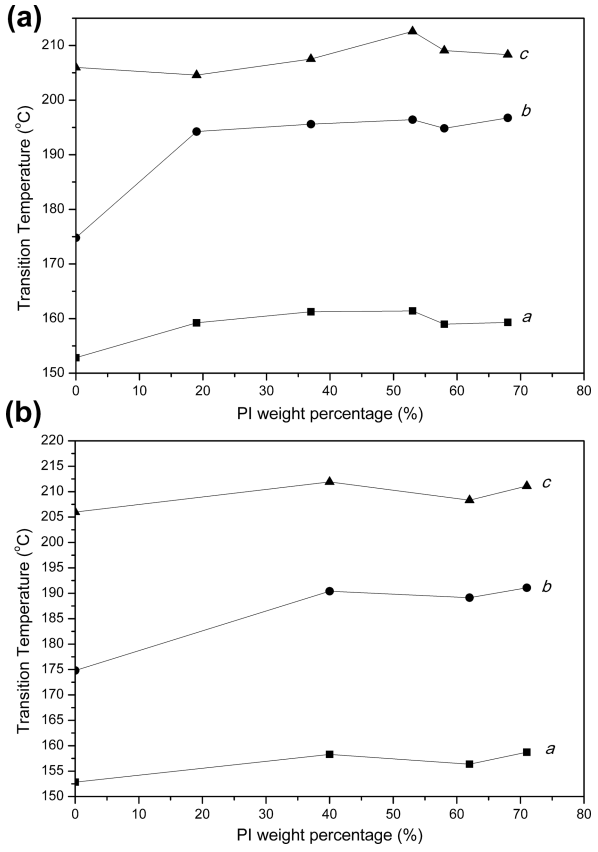

Figure 10. Peak temperatures of subtransitions *a*, *b*, and *c* in H(II) region during melting for (a) DBCPs and (b) TBCPs.

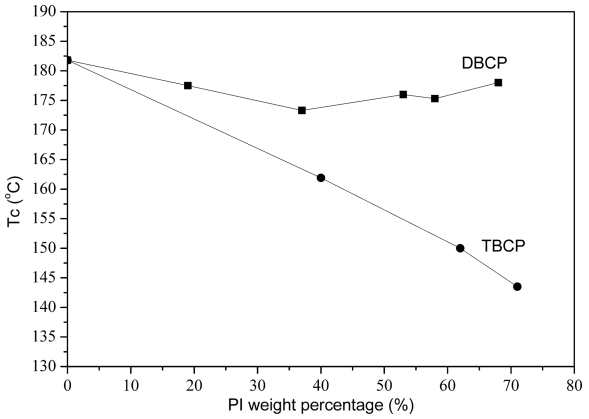

Figure 11. Crystallization temperature (T_c) of P3HT-PI BCPs against the weight percentage of PI.

crystallite size and the interdomain boundaries between P3HT and PI to restrict the movement of P3HT.

During cooling, two exothermic transitions were observed as the major one at higher temperature corresponded to crystallization of P3HT and the minor one at lower temperature suggested the packing of hexyl side chains. Unlike the melting behaviors showing three subtransitions, only one transition was detected for the crystallization and whose peak temperature was defined as the crystallization temperature (T_c). As illustrated in Figure 11, T_c of DBCPs was slightly lower than that of pristine P3HT and the increment of the weight fraction of PI did not have distinctive effect on T_c. On the other hand, T_c of TBCPs was significantly lowered with increasing PI content, suggesting the elongation of PI should hamper crystallization of P3HT in TBCPs but not in DBCPs.

The degree of crystallization (DC), suggesting the fraction of crystalline domains in the P3HT regions, could be evaluated via DSC studies. DC was calculated according to eq 1

$$\mathrm{DC} = \frac{\Delta H_m}{\Delta H_m^\circ}\frac{100\%}{w_{\mathrm{P3HT}}} \quad (1)$$

where ΔH_m is the total enthalpy of transition H(II) of a BCP while ΔH_m° corresponds to that of the pristine P3HT with DC = 100%. w_{P3HT} is the weight fraction of P3HT in a BCP.

It was found that the trends of DC against the PI content in BCPs (shown in Figure 8) are similar to the variation in crystallite size. In DBCPs, DC of D1 was very close to the pristine P3HT while the increment in PI content led to enhancement of DC in D2, which might associate with the enlarged crystallite size (from WAXS) and the straight interdomain boundaries to direct the growth of P3HT crystals. Nevertheless, the further increment in the weight fraction of PI would decrease DC slightly in D3−D5 despite the augmentation in crystallite size, suggesting the number of crystallites was suppressed which might result from the curved interdomain boundaries to suppress the formation of P3HT crystallites. By contrast, DC of P3HT in TBCPs was remarkably suppressed with the increasing weight fraction of PI, in good agreement with the decrement in crystallite size, further confirming the attachment of PI at both terminals of P3HT should severely restrict the packing of P3HT.

DOI: 10.1021/ma502417w
Macromolecules 2015, 48, 3269−3281

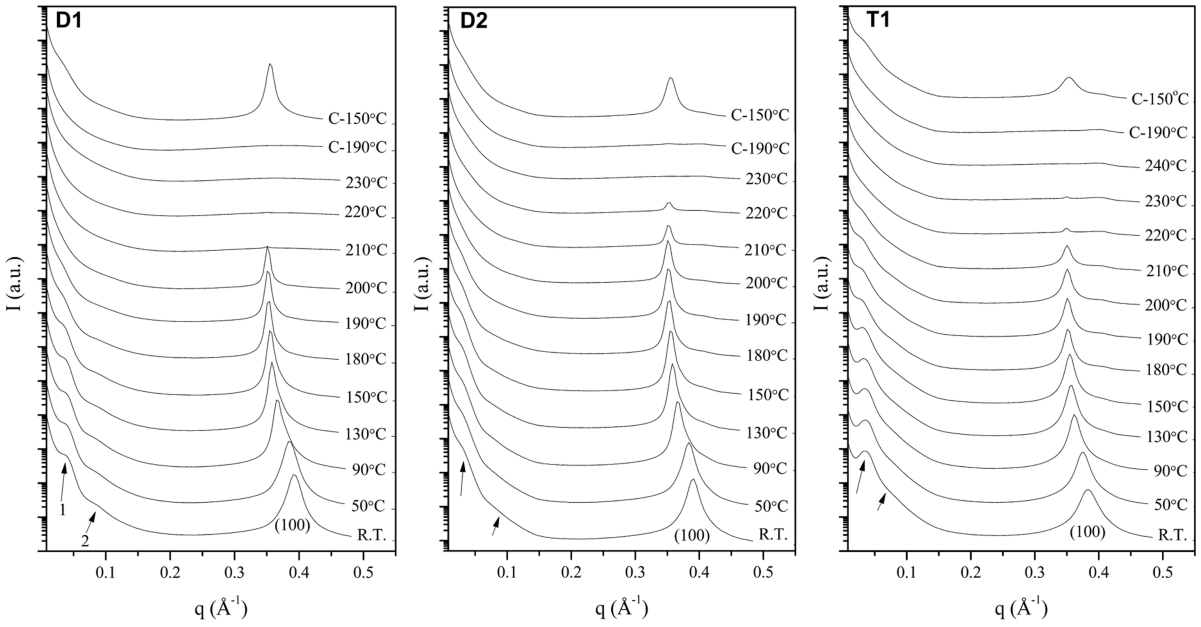

Figure 12. Temperature-dependent SAXS/WAXS patterns of D1, D2, and T1.

Proposed Model for Self-Assembly and Interplays between Morphology and Crystallinity. Previous studies of rod−coil diblock copolymers suggest that the morphology of these copolymers is governed by four parameters: the Flory−Huggins interaction, the Maier−Saupé interaction, the volume fraction of the coil segment, and the conformation asymmetry or scaling dimension mismatch between the rod and the coil segments. The Flory−Huggins interaction, represented by χN as χ is the Flory−Huggins parameter and N is the number of volumetric repeat units, measures the incompatibility between rod and coil segments. The Maier−Saupe interaction, referred as μN, generally suggests the strength of rod−rod interaction. The coil fraction f measures the relative volume of the two segments. The mismatch in scaling dimension between the rod and coil is represented in various forms in different studies, such as coil to rod length ratio ν or competition between rod and coil segments $G = \mu/\chi$.

Because of the difficulty in synthesizing well-defined rod−coil block copolymers with narrow molecular weight distribution, systematic studies on the quantitative information on μ and χ are limited. Segalman and co-workers performed a series of studies on poly(diethylhexyloxy-*p*-phenylenevinylene-*block*-isoprene) (PPV-*b*-PI) block copolymers, in which the Maier−Saupé (rod−rod) interaction parameter (μ) of PPV was extracted using a linear regression fitting to the nematic−isotropic transition at different molecular weight of pristine PPV with an assumption of pure rod conformation, and it could be expressed as $\mu = 183/T - 0.236$.[35] The χ value was obtained by fitting the interfacial segregation of block copolymer to a homopolymer interface with a self-consistent field theory (SCFT) simulation, and a temperature-dependent formula was suggested as $\chi = 34.8/T - 0.091$. The approach adopted in the study was different from the method using for most coil−coil BCPs by analyzing the structure factor of SAXS/SANS patterns measured in the disordered state at the temperatures above the order−disorder transition temperature (T_{ODT}) using the random phase approximation (RPA) assumption since the existence of complex aggregated structures in the melting states would lead to the inconsistency between theoretical and experimental results. According to the equation of μ and χ, μ was larger than χ by almost 50 times. Experimentally, lamellar phase with the orientation of lamellae correlated across several rods was the only morphology observed for PPV-*b*-PI with low N at all volume fraction of PI (f_{PI}), suggesting strong rod−rod interaction would dominate the assembly of PPV-*b*-PI in weak segregation regime.[36] When increasing N to increase segregation strength and geometric asymmetry between PPV and PI, hexagonally packed phases of rectangular PPV nanodomains embedded in the PI-rich matrix observed for the BCP with $f_{PI} > 0.87$.[37] Su and co-workers reported the phase diagram of poly(diethylhexyloxy-*p*-phenylenevinylene-*block*-methyl methacrylate) (PPV-*b*-PMMA) block copolymers, and they observed lamellar structures when $f_{PMMA} < 0.54$ while the PPV strips packed into hexagonal lattice as $f_{PMMA} > 0.66$. In contrast to PPV-*b*-PI BCPs, which showed T_{ODT} of the microphase-separated structure was lower than the nematic−isotropic transition temperature of PPV, the smectic packed PPV became isotropic at the temperature generally lower than or similar to T_{ODT}.[38] Although numerical information on χ was not available in this study, the microphase segregation strength between PPV and PMMA was believed to be greater than that between PPV and PI. Therefore, comparing to PPV-*b*-PI, lower coil fraction was required for PPV-*b*-PMMA to suppress the rod persistence length to form nonlamellar microstructure as well as reversible liquid crystalline and microphase phase transitions was observed.

In P3HT rod−coil block copolymers, studies on identification of the strengths of rod−rod interaction and rod−coil incompatibility were even rarer. Unlike PPV showing a relatively wide temperature range of nematic phase, the nematic window of P3HT is very narrow and difficult to be observed experimentally. Lin et al. suggested the Maier−Saupé parameter of P3HT as $\mu = 180/T - 0.3$ based on low molecular weight P3HT.[39] Accordingly, the rod−rod interaction of P3HT should be weaker as compared to PPV at the same temperature. In the same work, the Flory−Huggins parameter between P3HT and PMMA was also extracted from the structure factor of the SAXS pattern measured above T_{ODT} using random phase

DOI: 10.1021/ma502417w
Macromolecules 2015, 48, 3269−3281

Scheme 3. Proposed Models for Self-Assembly of P3HT-PI DBCPs and TBCPs at Different PI Fraction

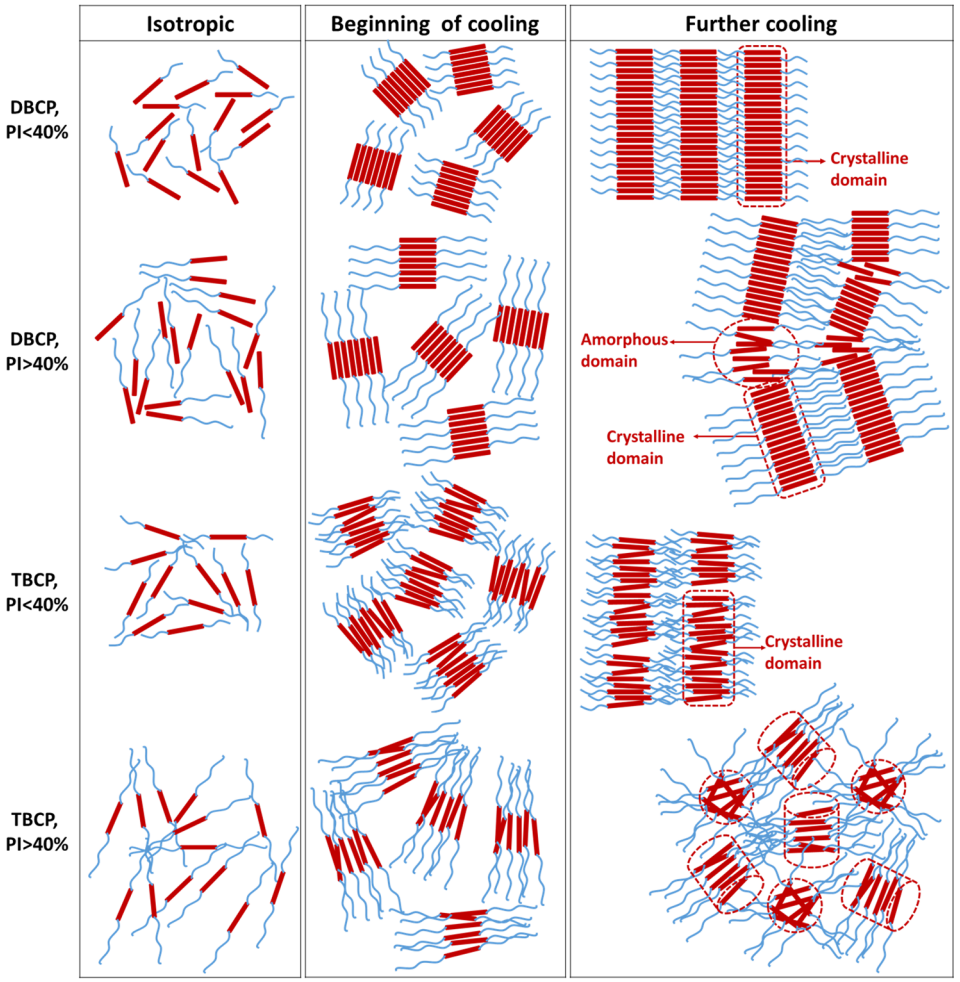

approximation (RPA) assumption of a P3HT-*b*-PMMA with f_{PMMA} = 0.49 and which was expressed as χ = 56.370/T + 0.0433. The strength of microphase segregation between P3HT and PMMA was much stronger than that between PPV and PI discussed previously and which should be also stronger than PPV−PMMA segregation.

To evaluate the strength of microphase separation between P3HT and PI, temperature-dependent SAXS/WAXS studies were performed on the thermal annealed D1 and D2. In the SAXS/WAXS patterns provided in Figure 12, the scattering signal at low q corresponding to microphase separation was lost at 200 °C during heating, suggesting the order−disorder transition should occur around 200 °C. On the other hand, the peak at high q signifying the (100) direction of the P3HT crystallite totally disappeared between 210 and 230 °C, indicating complete melting. The melting could be referred as crystalline−isotropic transition according to polarized optical microscopy (POM) as optical isotropy was revealed above this temperature range. Therefore, we might conclude that T_{ODT} was slightly lower than the isotropization temperature in P3HT-*b*-PI. The sequence and the temperature differentiation of ODT and anisotropy−isotropy transitions were similar to that of PPV-*b*-PI in moderate segregation regime. On the basis of the above discussions, we reasonably suggest the microphase segregation strength of P3HT-*b*-PI in this work should be stronger than PPV-*b*-PI but weaker than PPV-*b*-PMMA and P3HT-*b*-PMMA and which could be categorized into moderate segregation regime. However, P3HT-*b*-PI with high PI fraction in this work did not exhibit any microstructure similar to those observed in PPV-*b*-PI and PPV-*b*-PMMA with high coil fraction, indicating the self-assembly should be strongly influenced by factor other than the theoretically suggested four factors: χ, μ, f, and G.

We believe that crystallization of P3HT should play an important role in determining the morphology of P3HT BCPs. The morphologies were also found to closely relate to the crystallinity of P3HT within the BCPs. In PPV BCPs, PPV has a relatively wide temperature range of highly mobile nematic phase to allow PPV segments to organize corresponding to the rod−rod interaction. By contrast, P3HT tends to crystallize directly from an isotropic liquid without the privilege to assemble in the liquid crystalline phase so that crystallization might overwhelm the Maier−Saupé interaction in directing the morphology. For P3HT BCPs in weak phase segregation regime, short fibers or strips randomly oriented or packed with short-range order were generally observed owing to the dominance of fast crystallization of P3HT. For P3HT BCPs in strong phase segregation regime, microphase separation occurred at a temperature much higher than the crystallization temperature of P3HT, leading to morphologies with highly curved interdomain boundaries at high coil fraction and significantly suppressed crystallinity because of confined crystallization of P3HT. For example, P3HT-*b*-P2VP (poly(3-hexylthiophene-*block*-2-vinylpyridine)) with higher fraction of

DOI: 10.1021/ma502417w
Macromolecules 2015, 48, 3269−3281

P2VP exhibited blue-shifted optical absorption, decreasing melting point, and attenuated diffraction peaks in the WAXS pattern, which indicated a decrease in DC.[32] Similar phenomena was also observed in P3HT-*b*-PE (poly(3-hexylthiophene-*block*-ethylene).[40] Nevertheless, P3HT-*b*-PI BCPs in this work exhibited very different self-assembly behaviors in the thermal annealed bulk samples comparing to the previously reported P3HT BCPs. In DBCPs, only long fibers with sustainable crystallinity were observed for all samples with different fraction of PI. In the corresponding TBCPs with high PI content, short P3HT cylinders without long-range order and significantly suppressed crystallinity were revealed. Hereby we proposed the following mechanism mainly involving crystallization of P3HT and microphase segregation between P3HT and PI to explain the unique self-assembly of P3HT-PI BCPs, including the formation of the morphologies and the interplays between morphology and crystallinity. The proposed models for self-assembly of DBCPs and TBCPs are schematically illustrated in Scheme 3 for the ease of visualization.

During the thermal annealing processes, the samples were heated above 230 °C to ensure complete isotropy. The melts were then cooled down to 185 °C and annealed for 24 h under vacuum, a temperature slightly above the crystallization temperature of P3HT and over 200 K above the T_g of PI. In D1 and D2, microphase separation was moderate; therefore, P3HT would start to crystallize upon subsequent cooling and which should soon induce microphase separation as the scattering signals at both low q and high q could be observed in the temperature-dependent SAXS/WAXS patterns of D1 and D2 at 150 °C (the patterns labeled with C-150 °C). Since the interfacial areas between P3HT and PI domains tend to be minimized to decrease energetic penalties, the IDBs would like to straighten and extend if possible. Fortunately, PI was highly mobile during the whole cooling step so that the packing of P3HT could feasibly drag PI segments to accommodate the most energetic favorable molecular arrangement. When the PI content was low in DBCPs (D1 and D2), microphase separation should not be too strong to disturb the stacking of P3HT; as a consequence, P3HT segments would crystallize along the direction of IDBs between P3HT and PI domains to allow the formation of long straight fibers packed in a lamellar fashion. The straight and extended IDBs, on the other hand, also provide an encouraging environment for P3HT to crystallize, leading to enlarged crystallites and enhanced degree of crystallization. With the elongation of PI in DBCPs, the increasing microphase segregation strength (χN increased), and the entanglement of PI might start to perturb crystallization of P3HT, resulting in curved IDBs. However, long fibers with relatively good crystallinity could still be observed even at high PI content (D5), in contrast to short worms or cylinders of P3HT with significantly suppressed crystallinity exhibited by most P3HT BCPs with high coil contents. The preservation of crystallinity might be attributed to the high flexibility of PI since PI could still move promptly even at low temperatures to allow the stacking of P3HT, instead of considerably interfering crystallization of P3HT like other coil segment with high T_g.

In TBCPs, however, the stacking of P3HT segment was hindered due to more pronounced entanglement of two terminal PIs to restrict the movements of PI and thus to further limit the motion of P3HT. Therefore, P3HT in TBCPs exhibited much lower crystallization temperature and suppressed degree of crystallization as compared to P3HT in the corresponding DBCPs having similar PI fraction. Comparing T1 with D2 showing similar lamellar morphologies, the temperature-dependent SAXS/WAXS pattern of T1 (Figure 12) at 150 °C during cooling (C-150) displayed a stronger scattering signal at low q attributed to the lamellar microstructure and a weaker and broader peak at high q corresponding to the P3HT crystallites at (100) direction. During heating, the low q signal disappeared below 200 °C and the high q peak vanished at 230 °C for D2; while the low q signal retained until 210 °C and the high q peak became almost undetectable at 220 °C for T1. The closeness of T_{ODT} and the isotropization temperature in T1 as well as the stronger scattering signal attributed to microphase separation would suggest microphase segregation strength is stronger in T1 than that in D2. Moreover, the high q peak for D2 became narrower with increasing temperature during heating, suggesting better organization of P3HT crystallites upon thermal annealing. By contrast, the fwhm of the (100) peak of T1 remained almost unchanged during heating, indicating the crystallinity of TCBPs could not be improved after thermal annealing, which further confirmed the difficulty for P3HT in TBCPs to move. Because of the lost of the molecular mobility to accommodate the favorable morphology for crystallization and of stronger microphase segregation, TBCPs with higher PI fraction would exhibit morphologies, such as P3HT cylinders, similar to those of P3HT diblock copolymers in strong segregation regimes with low P3HT crystallinity.

EXPERIMENTAL SECTION

Materials. Tetrahydrofuran (THF) and toluene were freshly distilled from CaH_2 and sodium/benzophenone under nitrogen. Solvents for anionic polymerization (toluene and THF) were further distilled from the corresponding polystyryl anion solution. Isoprene was degassed and distilled from dibutylmagnesium (Aldrich, 1.0 M solution in heptane) prior to use. *tert*-Butylmagnesium chloride (2.0 M in diethyl ether), isopropylmagnesium chloride (2.0 M), *sec*-butyllithium (1.3 M in cyclohexane) *N*-methylformanilide, $POCl_3$, $Ni(dppp)Cl_2$, $Pd(PPh_3)_4$, 4-formylphenylboronic acid, K_2CO_3, I_2, NBS, 3-bromohexylthiophene, and 1-bromohexane were purchased from Aldrich and used as received.

Synthesis of 2-Bromo-3-hexyl-5-iodothiophene. A three-step reaction was carried out to synthesize 2-bromo-3-hexyl-5-iodothiophene from 3-bromothiophene, the monomer of P3HT, including (1) hexyl side-chain attachment at third position, (2) selective bromination at second position, and (3) iodination at the fifth position of the thiophene ring. High purity of monomer is crucial for producing P3HT with uniform H/Br end-groups. The detailed procedures of the syntheses are described as follows. Grignard reagent hexylmagnesium bromide was prepared in distilled ether purified with sodium benzophenone. 13.42 g (0.552 mol) of magnesium (based on 30 g of 3-bromohexylthiophene) was charged into a 500 mL Rotaflo flask with a magnetic stir bar, and it was then vacuum-dried for 30 min and filled with high-purity N_2. 300 mL of dried ether was directly distilled into the flask, and then vigorous stirring and ice bath were applied. 51.7 mL (0.368 mol) of 1-bromohexane was injected slowly into the reaction flask under N_2 purging. The ice bath was removed after 15 min stirring, and the dark gray mixture was stirred at room temperature for another 3 h. Meanwhile, 150 mg (2.76×10^{-4} mol) of $Ni(dppp)Cl_2$ was charged into another 500 mL Rotaflo flask and vacuum-dried for 20 min before charging with high-purity N_2. 30 g (0.1853 mol) of 3-bromothiophene was charged into the flask under N_2 purging. The above mixture of 3-hexylmagnesium bromide was transferred using a double-tip needle, and the mixture was allowed to react for 24 h. The reaction mixture was poured into MeOH, and the precipitates were washed with distilled water for several times. Crude product was dried with anhydrous magnesium sulfate and subjected to

DOI: 10.1021/ma502417w
Macromolecules 2015, 48, 3269−3281

vacuum distillation to afford 3-hexylthiophene. ^{1}H NMR (400 MHz, $CDCl_3$) δ, ppm: 7.23 (d, J = 4.89 Hz, 1H), 6.93 (d, J = 6.18 Hz, 2H), 2.62 (t, 2H), 1.62 (m, 2H), 1.31 (m, 6H), 0.88 (t, 3H).

3-Hexylthiophene (30 g, 0.1782 mol) was charged into 500 mL reaction flask equipped with a stir bar. 200 mL of THF was freshly distilled from sodium followed by the addition of *N*-bromosuccinimide (33.29 g, 0.1872 mol) at 0 °C. Reaction was carried out for at least 1 h in an ice bath and terminated with 10 wt % $Na_2S_2O_3$(aq). Most of THF was evaporated using a rotavapor before the mixture was extracted with ether and washed subsequently with 10 wt % $Na_2S_2O_3$(aq) and 10 wt % KOH(aq). The ether fraction was collected and dried with anhydrous magnesium sulfate. Ether was then removed by a rotavapor, and the residues were subjected to vacuum distillation (oil bath T = 120 °C, 3 × 10^{-3} Torr) to afford 2-bromohexylthiophene. ^{1}H NMR (400 MHz, $CDCl_3$) δ, ppm: 7.18 (d, J = 5.59 Hz, 1H), 6.78 (dd, J = 7.88, 4.23 Hz, 1H), 2.54 (m, 2H), 1.56 (m, 3H), 1.33 (m, 7H), 0.89 (td, J = 15.40, 7.67 Hz, 3H).

2-Bromo-3-hexylthiophene (30 g, 0.1213 mol) was put into a 500 mL reaction flask followed by the addition of 300 mL of dichloromethane. Iodine (14.63g, 0.057 mol) and iodobenzene diacetate (19.496 g, 0.060) were added subsequently at 0 °C, and the mixture was stirred for overnight at room temperature. Reaction was quenched by addition of 10 wt % $Na_2S_2O_3$. Dichloromethane was evaporated to afford the crude product, which was then dissolved in ether and washed several times with 10 wt % $Na_2S_2O_3$(aq). By removing ether and vacuum drying, the purified 2-bromo-3-hexyl-5-iodothiophene was obtained. ^{1}H NMR (400 MHz, $CDCl_3$) δ, ppm: 6.97 (m, 1H), 2.51 (m, 2H), 1.52 (m, 4H), 1.30 (m, 7H), 0.89 (t, J = 6.76 Hz, 3H).

Syntheses of Aldehyde End-Functionalized P3HT: P3HT-H/CHO and P3HT-CHO/CHO. P3HT with bromine at one terminal thiophene and hydrogen at other terminal thiophene (P3HT-H/Br) was synthesized using the Yokozawa method as described below. 2-Bromo-3-hexyl-5-iodothiophene (4 g, 0.0107 mol) was charged into a 500 mL Rotaflo flask equipped with a stir bar and was vacuumed for 30 min. Freshly distilled THF (200 mL) was added under a nitrogen atmosphere, and the solution was then cooled to 0 °C. Isopropylmagnesium chloride (205 mL, 0.0102 mol) was injected via an airtight syringe, and the mixture was allowed to react for 30 min under an ice bath. The reaction mixture was then poured into a copious amount of methanol to afford purple precipitates, which was then collected and washed using Soxhlet extraction with methanol to produce purified P3HT-H/Br. The molecular weight of the synthesized P3HT-H/Br was suggested by GPC, and the purity of the end groups was identified by MALDI-TOF-MS.

P3HT-H/Br (1 g, 0.125 mmol), 4-formylphenylboronic acid (0.3749 g, 2.5 mmol), and K_2CO_3 (0.3455 g, 2.5 mmol) were charged into a reaction flask and vacuum-dried. 250 mL of distilled THF was then added under nitrogen, and the resulting mixture was stirred until a clear solution was obtained. $Pd(PPh_3)_4$ was added, and then the mixture was refluxed at 70 °C for 24 h under N_2. The Suzuki coupling reaction was then terminated by adding 2.5 mL of water. The reaction mixture was poured into methanol to afford the crude product, which was then subjected to Soxhlet extraction with methanol to afford purified P3HT-H/CHO—P3HT with hydrogen at one terminal and benzaldehyde at another terminal. The synthesis of P3HT-CHO/CHO from P3HT-H/Br, P3HT with both terminals being aldehyde, was performed according to our previous work.[19] MALDI-TOF-MS and ^{1}H NMR studies were performed to evaluate the completeness of end-functionalization (yield: 97%).

General Procedure for Syntheses of P3HT-*b*-PI Diblock Copolymers (DBCPs) and PI-*b*-P3HT-*b*-PI Triblock Copolymers (TBCPs). P3HT-H/CHO (0.3 g, 0.04 mmol) was charged into a 100 mL Rotaflo flask and vacuum-dried for 2 days before being dissolved in 80 mL of freshly distilled toluene purified with living polystyryl anions. Polyisoprene in 1,4-addition (5 equiv) was synthesized from anionic polymerization in toluene at room temperature under the atmosphere of nitrogen. *sec*-BuLi (0.165 mL, 0.2 mmol) [1.3 M] in cyclohexane was injected into freshly distilled toluene and followed by the addition of purified isoprene (0.88 mL) distilled from dibutylmagnesium. The polymerization was performed for 1 day at room temperature, and the P3HT-H/CHO toluene solution was then transferred into the solution of PI anions. The resulting mixture was stirred for 3 h at room temperature to allow the coupling reaction between the terminal aldehyde of P3HT-H/CHO and anionic PI before being quenched with 1 mL of anhydrous methanol. Toluene in the reaction mixture was removed by a rotavapor, and ethyl acetate (100 mL) was then added. The precipitate was the crude product of BCP, and excess PI was dissolved in ethyl acetate. The precipitate was collected after centrifugation and washed with ethyl acetate. The yield was around 70%. For TBCP, the same procedure was adopted on P3HT-CHO/CHO instead of P3HT-H/CHO.

Instruments. The molecular weight of polymers was determined using a Viscotek gel permeation chromatograph equipped with UV, RI, and RALS detector. ^{1}H NMR spectra were obtained using a Bruker Advance 400 MHz spectrometer with *d*-chloroform as solvent. MALDI-TOF MS spectra were obtained using a Voyager DE-PRO MALDI-TOF-MS (Applied Biosystems, Austin, TX) equipped with a N_2 laser (337 nm). Cryo-ultramicrotomy was done with a Leica Ultracut S with cryo-tank. Ultrathin sections (around 100 nm) were obtained with a Leica Ultracut UCT6 and then deposited onto grid and subjected to transmission electron microscopy analysis on JEOL JEM-1400 operating at 80 kV. SAXS and WAXS measurements were conducted on NSRRC (Hsinchu, Taiwan) beamline 23A, 17A, and 13A. DSC was performed by using a TA Q200 with scanning rate of 10 °C/min.

■ CONCLUSION

In this work, P3HT−polyisoprene (P3HT-PI) diblock and triblock copolymers having designated molecular architecture with accurately controlled molecular weight and composition were successfully synthesized via efficient coupling reaction between aldehyde end-functionalized P3HT and living anioinic polysioprene. The self-assembly behaviors of the diblock copolymers appeared very different from most of the published P3HT rod−coil block copolymer systems, showing elongated fibers with preserved P3HT crystallinity. The most noteworthy finding was D2, the DBCP containing 37 wt % of PI, exhibiting long straight strips with concurrently enhanced P3HT crystallinity arranging in a parallel fashion. The unique self-assembly could be attributed to the high flexibility of PI and the moderate microphase separation between P3HT and PI to conduct the crystallization of P3HT. By contrast, the TBCPs exhibited morphologies of lamellae and short P3HT cylinders with suppressed P3HT crystallinity since the two terminal PI segments might undergo more pronounced entanglement to restrict the chain movement, thus hampering the packing of P3HT.

■ ASSOCIATED CONTENT

Ⓢ Supporting Information

Table S1 and Figure S1. The Supporting Information is available free of charge on the ACS Publications website at DOI: 10.1021/ma502417w.

■ AUTHOR INFORMATION

Corresponding Author

*E-mail cychao138@ntu.edu.tw (C.-Y.C.).

Notes

The authors declare no competing financial interest.

■ ACKNOWLEDGMENTS

The authors thank Prof. Jing-Jong Shyue and Academia Sinica for MALDI-TOF-MS measurements. The financial support from Ministry of Science and Technology (previously known as

DOI: 10.1021/ma502417w
Macromolecules 2015, 48, 3269−3281

National Science Council, NSC) of Taiwan is gratefully acknowledged.

REFERENCES

(1) Briseno, A. L.; Mannsfeld, S. C. B.; Jenekhe, S. A.; Bao, Z.; Xia, Y. *Mater. Today* **2008**, *11* (4), 38−47.
(2) Heeger, A. J. *J. Phys. Chem. B* **2001**, *105* (36), 8475−8491.
(3) Ma, W.; Yang, C.; Gong, X.; Lee, K.; Heeger, A. J. *Adv. Funct. Mater.* **2005**, *15* (10), 1617−1622.
(4) O'Neill, M.; Kelly, S. M. *Adv. Mater.* **2011**, *23* (5), 566−584.
(5) Sirringhaus, H. *Adv. Mater.* **2009**, *21* (38−39), 3859−3873.
(6) Sirringhaus, H.; Tessler, N.; Friend, R. H. *Science* **1998**, *280* (5370), 1741−1744.
(7) Wang, F.; Yang, Y.; Swager, T. M. *Angew. Chem.* **2008**, *120* (44), 8522−8524.
(8) Cho, S.; Lee, K.; Yuen, J.; Wang, G.; Moses, D.; Heeger, A. J.; Surin, M.; Lazzaroni, R. *J. Appl. Phys.* **2006**, *100* (11), 114503.
(9) Miller, S.; Fanchini, G.; Lin, Y.-Y.; Li, C.; Chen, C.-W.; Su, W.-F.; Chhowalla, M. *J. Mater. Chem.* **2008**, *18* (3), 306−312.
(10) Kim, D. H.; Han, J. T.; Park, Y. D.; Jang, Y.; Cho, J. H.; Hwang, M.; Cho, K. *Adv. Mater.* **2006**, *18* (6), 719−723.
(11) Rahimi, K.; Botiz, I.; Stingelin, N.; Kayunkid, N.; Sommer, M.; Koch, F. P. V.; Nguyen, H.; Coulembier, O.; Dubois, P.; Brinkmann, M.; Reiter, G. *Angew. Chem., Int. Ed.* **2012**, *51* (44), 11131−11135.
(12) Zhao, K.; Xue, L.; Liu, J.; Gao, X.; Wu, S.; Han, Y.; Geng, Y. *Langmuir* **2009**, *26* (1), 471−477.
(13) Li, L.; Lu, G.; Yang, X. *J. Mater. Chem.* **2008**, *18* (17), 1984−1990.
(14) Botiz, I.; Martinson, A. B. F.; Darling, S. B. *Langmuir* **2010**, *26* (11), 8756−8761.
(15) Botiz, I.; Darling, S. B. *Macromolecules* **2009**, *42* (21), 8211−8217.
(16) Moon, H. C.; Anthonysamy, A.; Kim, J. K.; Hirao, A. *Macromolecules* **2011**, *44* (7), 1894−1899.
(17) Higashihara, T.; Ohshimizu, K.; Hirao, A.; Ueda, M. *Macromolecules* **2008**, *41* (24), 9505−9507.
(18) Dai, C.-A.; Yen, W.-C.; Lee, Y.-H.; Ho, C.-C.; Su, W.-F. *J. Am. Chem. Soc.* **2007**, *129* (36), 11036−11038.
(19) Lim, H.; Huang, K.-T.; Su, W.-F.; Chao, C.-Y. *J. Polym. Sci., Part A: Polym. Chem.* **2010**, *48* (15), 3311−3322.
(20) Lim, H.; Ho, C.-C.; Wu, S.-J.; Tsai, H.-C.; Su, W.-F.; Chao, C.-Y. *Chem. Commun.* **2013**, *49* (80), 9146−9148.
(21) Deribew, D.; Pavlopoulou, E.; Fleury, G.; Nicolet, C.; Renaud, C.; Mougnier, S.-J.; Vignau, L.; Cloutet, E.; Brochon, C.; Cousin, F.; Portale, G.; Geoghegan, M.; Hadziioannou, G. *Macromolecules* **2013**, *46* (8), 3015−3024.
(22) Loewe, R. S.; Khersonsky, S. M.; McCullough, R. D. *Adv. Mater.* **1999**, *11* (3), 250−253.
(23) Chen, T. A.; Rieke, R. D. *J. Am. Chem. Soc.* **1992**, *114* (25), 10087−10088.
(24) Yokoyama, A.; Miyakoshi, R.; Yokozawa, T. *Macromolecules* **2004**, *37* (4), 1169−1171.
(25) Miyakoshi, R.; Yokoyama, A.; Yokozawa, T. *J. Am. Chem. Soc.* **2005**, *127* (49), 17542−17547.
(26) Lohwasser, R. H.; Thelakkat, M. *Macromolecules* **2011**, *44* (9), 3388−3397.
(27) Liu, J.; McCullough, R. D. *Macromolecules* **2002**, *35* (27), 9882−9889.
(28) Wu, Z.; Petzold, A.; Henze, T.; Thurn-Albrecht, T.; Lohwasser, R. H.; Sommer, M.; Thelakkat, M. *Macromolecules* **2010**, *43* (10), 4646−4653.
(29) Yuan, Y.; Zhang, J.; Sun, J.; Hu, J.; Zhang, T.; Duan, Y. *Macromolecules* **2011**, *44* (23), 9341−9350.
(30) Pankaj, S.; Beiner, M. *Soft Matter* **2010**, *6* (15), 3506−3516.
(31) Causin, V.; Marega, C.; Marigo, A.; Valentini, L.; Kenny, J. M. *Macromolecules* **2004**, *38* (2), 409−415.
(32) Lee, Y.-H.; Yen, W.-C.; Su, W.-F.; Dai, C.-A. *Soft Matter* **2011**, *7* (21), 10429.
(33) Zhao, Y.; Yuan, G.; Roche, P.; Leclerc, M. *Polymer* **1995**, *36* (11), 2211−2214.
(34) Winokur, M. J.; Spiegel, D.; Kim, Y.; Hotta, S.; Heeger, A. J. *Synth. Met.* **1989**, *28* (1−2), 419−426.
(35) Olsen, B. D.; Shah, M.; Ganesan, V.; Segalman, R. A. *Macromolecules* **2008**, *41* (18), 6809−6817.
(36) Olsen, B. D.; Segalman, R. A. *Macromolecules* **2005**, *38* (24), 10127−10137.
(37) Olsen, B. D.; Segalman, R. A. *Macromolecules* **2007**, *40* (19), 6922−6929.
(38) Ho, C.-C.; Lee, Y.-H.; Dai, C.-A.; Segalman, R. A.; Su, W.-F. *Macromolecules* **2009**, *42* (12), 4208−4219.
(39) Lin, S.-H.; Wu, S.-J.; Ho, C.-C.; Su, W.-F. *Macromolecules* **2013**, *46* (7), 2725−2732.
(40) Müller, C.; Radano, C. P.; Smith, P.; Stingelin-Stutzmann, N. *Polymer* **2008**, *49* (18), 3973−3978.

DOI: 10.1021/ma502417w
Macromolecules 2015, 48, 3269−3281